Sub-Nyquist computational ghost imaging with orthonormal spectrum-encoded speckle patterns

Xiaoyu Nie, ^{1,2} Xingchen Zhao ⁰, ¹ Tao Peng ¹, ^{1,*} and Marlan O. Scully ^{1,3}

¹Institute for Quantum Science and Engineering, Texas A&M University, College Station, Texas 77843, USA

²School of Physics, Xi'an Jiaotong University, Xi'an, Shaanxi 710049, China

³Baylor University, Waco, Texas 76706, USA

(Received 27 February 2022; accepted 18 April 2022; published 27 April 2022)

Computational ghost imaging generally requires a large number of patterns to obtain a high-quality result. It has been shown that both premodulated orthogonal patterns and postprocessing orthonormalization improve imaging quality and reduce the required pattern number. In this work, we propose and experimentally demonstrate a sub-Nyquist computational ghost imaging technique using the orthonormal spectrum-encoded speckle patterns. Our method enables the reconstruction of grayscale images at very low sampling ratios. Additionally, we show that this technique can be combined with compressive sensing to enhance image quality further. Reconstructed images are analyzed using quality indicators such as mean-square error, signal-to-noise ratio, correlation coefficient, and mean-square error of the detected edge. With our method, high-quality images can be obtained at a sampling ratio significantly lower than conventional methods.

DOI: 10.1103/PhysRevA.105.043525

I. INTRODUCTION

Computational ghost imaging (CGI) [1,2], an ameliorated scheme on traditional ghost imaging (GI) [3–5], owns the ability to reconstruct the object via a single-pixel detector. CGI grants advantages in an expanding range of nonconventional applications such as wide spectrum imaging [6,7] and depth mapping [8,9]. It also finds application to various fields, such as temporal imaging [10], x-ray imaging [11], and remote sensing [12]. However, it usually requires the number of speckle patterns used in CGI to be much greater than the total number of pixels in the speckle pattern in order for good quality imaging to be obtained, which is time-consuming and resource intensive. Furthermore, it produces limitations such as only being suitable for static object reconstruction.

The problem has been addressed by a number of methods. Compressing sensing (CS) is a well-known technique for reducing the required sampling ratio by exploring sparsity properties [13,14]. Nevertheless, it is strictly limited by the sparsity of the image. Deep learning has also demonstrated its ability to achieve sub-Nyquist ghost imaging [15–17]. One limitation is that most of the networks are trained by experimental CGI results, and therefore numerous measurements have to be done in advance. Also, the training inputs and the training environment for image reconstruction should be almost identical to the experiment to make the system effective. Furthermore, only simple objects can be imaged with deep learning based ghost imaging techniques, which restricts its application. The use of CGI with an orthonormal pattern, such as the Hadamard pattern or Fourier basis pattern, can also reduce sampling ratios [18–20]. In particular, Luo et al. introduced a data postprocessing algorithm to improve the

reconstruction process in a GI system with pseudothermal light [21]. The required number of speckle patterns is reduced by applying the Gram-Schmidt process to the speckle patterns and the intensity sequence collected by the bucket detector. However, such a method is sensitive to noise, and the image quality is not comparable with standard CGI when the sampling ratio is high, due to the information loss during the postprocessing. Gaussian white-noise patterns are typically used for GI. These speckle patterns have a flat spectrum over the range of spatial frequencies. Our recent development involves customizing the power spectrum distribution of speckle patterns to realize superresolution and noise robustness in an imaging system [22,23]. In contrast to white noise, these speckle patterns generally have unique spectrum distributions and nonzero cross-correlations between adjacent pixels.

In this work, we present a method on generating orthonormal spectrum-encoded speckle patterns, which can significantly reduce the CGI experiment sampling ratio. In addition, the CS algorithm is used in combination with the speckle patterns to enhance imaging quality further. We also compare the orthonormal spectrum-encoded pattern GI (OSGI), sequential Hadamard pattern GI (SHGI), orthonormal white-noise pattern GI (OWGI), traditional white-noise pattern GI (WGI), and their corresponding CS-combined methods OSGI-CS, SHGI-CS, OWGI-CS, and WGI-CS. The results are tested using the quality indicators such as the meansquare error (MSE), signal to noise ratio (SNR), correlation coefficient (CC), and MSE of the detected edge [21,24,25]. The first three indicators evaluate the overall quality of the images, and edge detection is to find the boundaries of objects within images, which is particularly useful in extracting the feature of the images. Our results show that OSGI always performs well in the non-CS amelioration CGI system and OSGI-CS further maximizes its quality, at very low sampling ratios. As a matter of fact, the sampling ratio may be reduced

^{*}taopeng@tamu.edu

one order lower, while the image quality is still better as compared to the standard CGI. Additionally, it suggests an optimal choice of different orthonormal methods with different sampling ratios when noise is present.

II. ORTHONORMAL SPECTRUM-ENCODED SPECKLE PATTERNS

Most natural images are apparently different in the spatial distribution, but share a common feature in the frequency domain, i.e., their spatial frequencies tend to be concentrated on the low-frequency parts [26,27]. Therefore, it is natural to seek speckle patterns that emphasize the low-frequency components, especially when the sampling ratio is low. Meanwhile, these patterns are better on an orthogonal basis in the spatial frequency domain to cover the entire frequency range efficiently. Here we present a general generation method for this type of speckle pattern. Firstly, a group of low-frequency dominated speckle patterns should be generated by filtering random white noise in the Fourier spectrum. For example, the initial speckle patterns are generated by applying a ω^{-1} filter (or any low-pass filter) on the ω^0 white-noise patterns in the Fourier domain. Then, the inverse Fourier transformation upon the filtered spectrum will deliver a group of the low-frequency dominated speckle patterns with random-phase matrices assigned to each pattern. The Gram-Schmidt process is then performed to orthonormalize the patterns. The initial patterns are represented by matrices $P_1, P_2, P_3, \dots, P_N$, and the orthonormal patterns are represented by matrices $\widetilde{P}_1, \widetilde{P}_2, \widetilde{P}_3, \dots, \widetilde{P}_N$, all of which contain 64×128 elements. We define the projection coefficient as $c_{mn} = \frac{\langle P_m, \widetilde{P}_n \rangle_F}{\langle \widetilde{P}_n, \widetilde{P}_n \rangle_F}$, where \langle , \rangle_F denotes Frobenius inner product operation. The orthonormal patterns can be generated by

$$\widetilde{P}_1 = P_1, \quad \widetilde{P}_m = P_m - \sum_{n=1}^{m-1} c_{mn} \widetilde{P}_n.$$
 (1)

Then, we renormalize the histogram of $\widetilde{P_1},\widetilde{P_2},\widetilde{P_3},\ldots,\widetilde{P_N}$ to [0, 255], which we define as \widetilde{P}_1' , \widetilde{P}_2' , \widetilde{P}_3' , ..., \widetilde{P}_N' . According to the number of orthogonal vector space, we generate 8192 patterns for each kind, which is equal to the number of total pixels in a single pattern. We thus have a complete set of orthonormal patterns. After the orthonormalization, the spatial frequency distribution of the speckle patterns tends to shift from their initial low frequency to high frequency. The later the speckle patterns in the orthonormalization process, the greater the frequency shift, as shown in Fig. 1. We also perform the orthonormalization process to the white-noise patterns for OWGI measurements as a comparison. These patterns still exhibit the white-noise characteristic, i.e., each pattern is still uniformly distributed over the frequency range. Alternatively, each of the orthonormal spectrum-encoded patterns has its own spatial frequency distribution. All the distributions of a complete set result in a uniform distribution in the spatial frequency. We note here that, unlike the postprocessing method shown in [21], we directly generate these orthonormal patterns but with heterogeneous spatial frequency distribution and apply them to the digital micromirror device (DMD). Therefore, the orthonormalization coefficients and patterns are made at once. Besides, we do not have any intensity losses

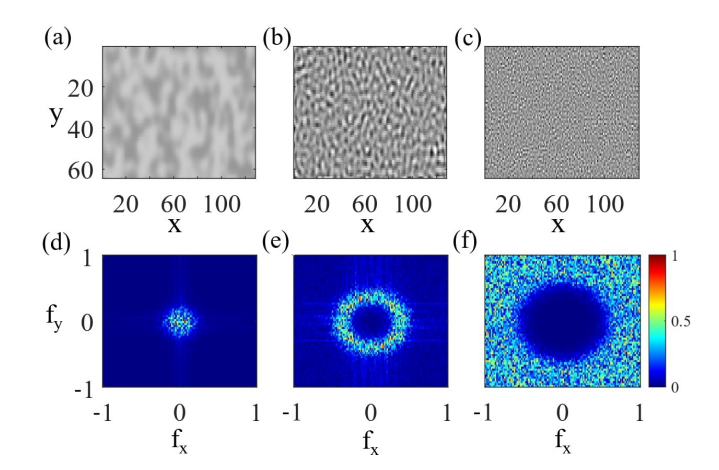


FIG. 1. The orthonormal spectrum-encoded speckle patterns: (a) the 1st pattern, (b) the 1000th pattern, and (c) the last pattern (8192nd). The *x*- and *y*-axis are coordinates of the pixel numbers; (d), (e), and (f) are normalized spatial frequency distributions of the 1st pattern, the 1000th pattern, and the 8192nd pattern, respectively. The *x*- and *y*-axis are coordinates of the normalized spatial frequencies.

during the orthonormalization process. In our scheme, the intensity is measured as $I_i = \langle T, \widetilde{P}'_i \rangle_F$, where T represents the spatial transmission coefficient matrix of the object and \widetilde{P}'_i is the ith orthonormal pattern. The image is then retrieved by calculating the correlation pattern $\Gamma^{(2)}$, a matrix that maintains the same dimensions and size as the patterns, between patterns and collected light intensity sequence as

$$\Gamma^{(2)} = \frac{1}{N} \sum_{i=1}^{N} I_i \widetilde{P}_i' - \frac{1}{N^2} \sum_{i=1}^{N} I_i \sum_{i=1}^{N} \widetilde{P}_i',$$
 (2)

where *N* is the number of speckle patterns. The sampling ratio is then defined as $\beta = N/N_{\text{pixel}}$.

We investigate the spatial frequency, autocorrelation, and cross-correlation properties of the orthonormal spectrumencoded speckle pattern. As shown in Fig. 1, the frequency peak moves to the higher end when the pattern number increases. Under orthonormalization, the pattern gradually transits from low- to high-frequency dominated distribution. This is apparent since the orthonormalization protocol naturally involves the spatial frequency domain. Consequently, these types of speckle patterns keep the low frequency in domination when β is small. Their corresponding high and broad cross-correlation gives a great advantage in noise suppression and signal boost. Later, they can enhance the resolution continuously as β increases. Indeed, both OSGI and SHGI own the OWGI's feature when β approaches 1, as shown in Fig. 2. A random pixel p(x, y) is chosen and its autocorrelation and cross-correlation with all other pixels are calculated. The cross-autocorrelation ratio R_{ca} is defined as

$$R_{\rm ca} = \frac{\Gamma_{p(x-1,y)}^{(2)} + \Gamma_{p(x+1,y)}^{(2)} + \Gamma_{p(x,y-1)}^{(2)} + \Gamma_{p(x,y+1)}^{(2)}}{4\Gamma_{p(x,y)}^{(2)}}.$$
 (3)

The pink line in Fig. 2 shows that the cross-autocorrelation ratio is gradually dwindling. The cross-correlation starts from nearly 1 when β is small. It then gradually decreases to 0 when $\beta=1$, the same as the white-noise speckle pattern. From the

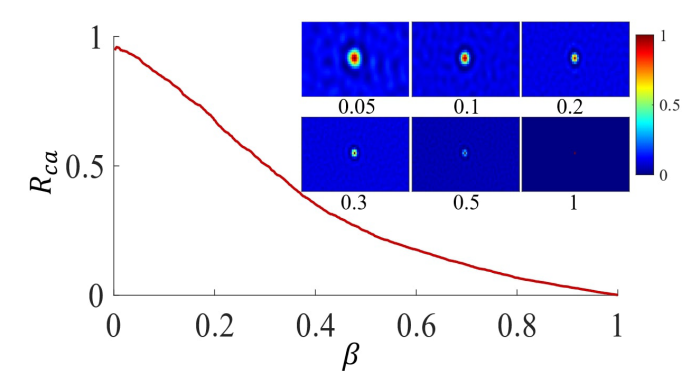


FIG. 2. The ratio of the cross-correlation and autocorrelation R_{ca} as a function of the sampling ratio β . Inset pictures: 2D plotted autoand cross-correlation of 5%, 10%, 20%, 30%, 50%, and 100% total pattern number over full patterns, respectively.

spatial frequency distribution of an arbitrary pattern, we can precisely predict the change of result during the image retrieving process with the spatial correlation. It is also expected that the OSGI, SHGI, and OWGI measurements will converge to the same results when β approaches 1, as shown in the following.

III. SIMULATION RESULTS

To test the feasibility of the OSGI method, we firstly perform simulation with part of a sample image "girl" as the object with total pixels of 64×128 . The simulation is done in the ideal condition without any noise. As shown in Fig. 3, OSGI gives an image result when the sampling ratio is only 5%, and a clear image at 20%. On the other hand, we see SHGI can give clear results around 20%, and become comparable with OSGI at 50%. OWGI only give a

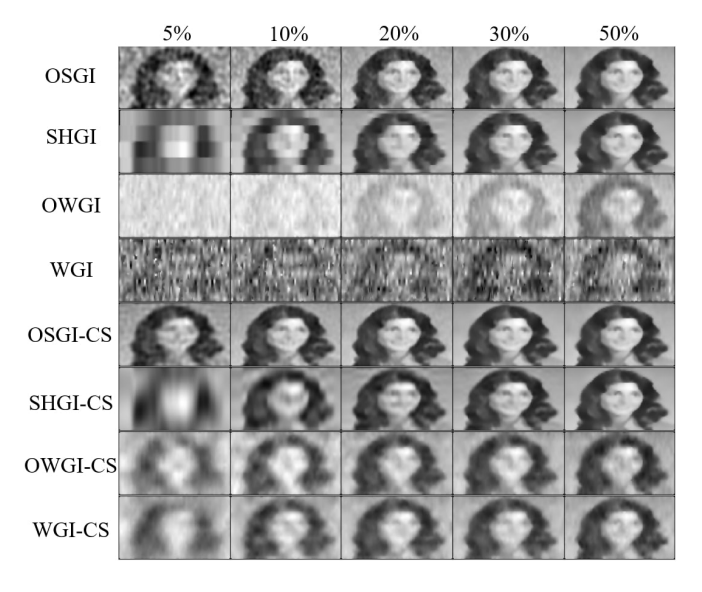


FIG. 3. Reconstructed images with sampling ratios from 5% to 50%. The simulation is done with various speckle patterns (OSGI, SHGI, OWGI, and WGI), and the corresponding results processed with compressive sensing algorithms. The total pixel in the image is 64×128 .

blurred image at 50% with a noisy background. Traditional WGI cannot retrieve the image even at the sampling ratio of 50%. A direct comparison between OSGI and OWGI suggests that the orthonormal process in the spatial frequency domain is essential for this method. By implementing the CS algorithm, we notice that the image quality is in general improved for all the methods. The image quality of SHGI-CS is also slightly improved as compared to SHGI. We also notice that the CS technique will improve the imaging quality of WGI and OWGI by giving a blurred image at 50%, which is not at all comparable to OSGI and OSGI-CS. The simulation results thus suggest that OSGI and OSGI-CS have the best performances in the sub-Nyquist sampling region.

To better judge the performance of various methods, we utilize four evaluating indicators of image quality, i.e., MSE, SNR, CC, and edge MSE, which are defined as

MSE =
$$\frac{1}{N_{\text{pixel}}} \sum_{i=1}^{N_{\text{pixel}}} (R_i - G_i)^2$$
, (4)

SNR =
$$10 \log_{10} \left(\frac{\sum_{i} R_{i}}{\sum_{i} |R_{i} - G_{i}|} \right)$$
, (5)

$$CC = \frac{Cov(R, G)}{\sqrt{Var(R)Var(G)}},$$
 (6)

$$CC = \frac{Cov(R, G)}{\sqrt{Var(R)Var(G)}},$$
(6)

and

$$MSE_{edge} = \frac{1}{N_{edge}} \sum_{j=1}^{N_{edge}} (R'_j - G'_j)^2.$$
 (7)

Here R represents the imaging result, G represents the ground truth. Var(·) is the variance of its arguments, and $Cov(\cdot)$ is the covariance of its arguments. R'_i is the extracted edge of the imaging result, and G'_{i} is the extracted edge of the ground truth. Here, we use the Sobel edge detection, a sophisticated built-in function in MATLAB [28].

As shown in Fig. 4, OSGI-CS and OSGI are better than other methods while β is below 40%. While the quality of OSGI increases with the increase of β , the image quality of OSGI-CS has a peak around $\beta = 30\%$, then starts to decrease. This is mainly due to the saturation of the image quality at such a low sampling ratio. The imaging result will then be overfitted by CS. We note here that SHGI performs better than WGI and OWGI, but worse than OSGI especially at low sampling ratio. When the sampling ratio approaches 1, these two methods are almost identical since they are both orthonormal patterns. SHGI-CS outperforms other methods as β reaches 50%, but it also has an overfitting problem. It is obvious that OWGI and WGI perform poorly with all sampling ratios. In the ideal condition, the orthonormalization process on the low-frequency dominated speckle patterns ultimately maximizes the information encoding-decoding efficiency, either in low sampling ratio with OSGI, OSGI-CS or in high sampling ratio with SHGI, SHGI-CS.

IV. EXPERIMENTAL RESULTS

We then experimentally test our scheme. The experimental setup is shown in Fig. 5. This is a typical CGI setup: A CW laser illuminates the DMD, where the speckle patterns with designed distributions are loaded. The pattern generated by

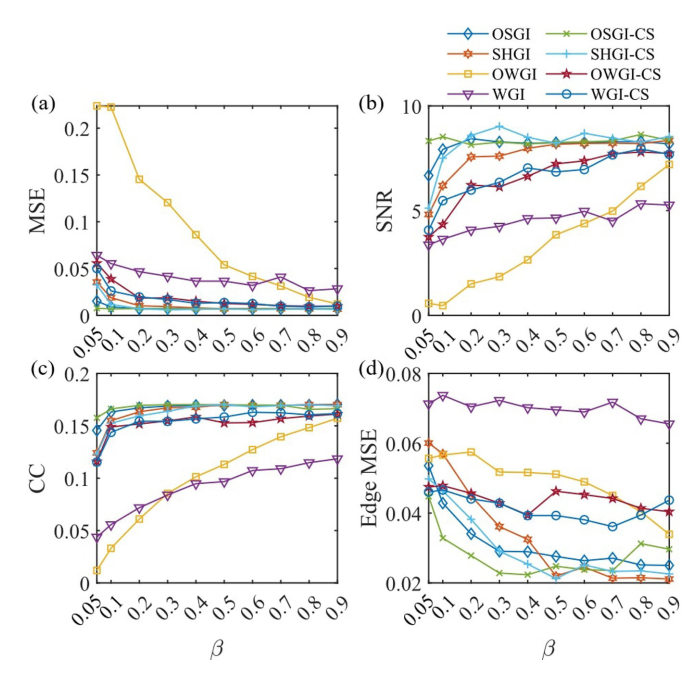


FIG. 4. Evaluation on simulation results based on the OSGI, SHGI, OWGI, WGI, OSGI-CS, SHGI-CS, OWGI-CS, and WGI-CS methods. Image qualities via different sampling ratio are given by (a) MSE, (b) SNR, (c) CC, and (d) Edge MSE.

the DMD is then projected onto the object plane. A bucket detector [simulated with a complementary metal-oxide semi-conductor (CMOS) camera MQ022CG-CM by adding all the pixel values of the active area] is put right after the object to record the transmitted light intensity. The DMD contains micromirrors, each of which is $16 \ \mu m \times 16 \ \mu m$ in size. Each speckle pattern has $N_{\rm pixel} \equiv N_x \times N_y$ independent pixels in the experiment, and each independent pixel consists of 10×10 micromirrors.

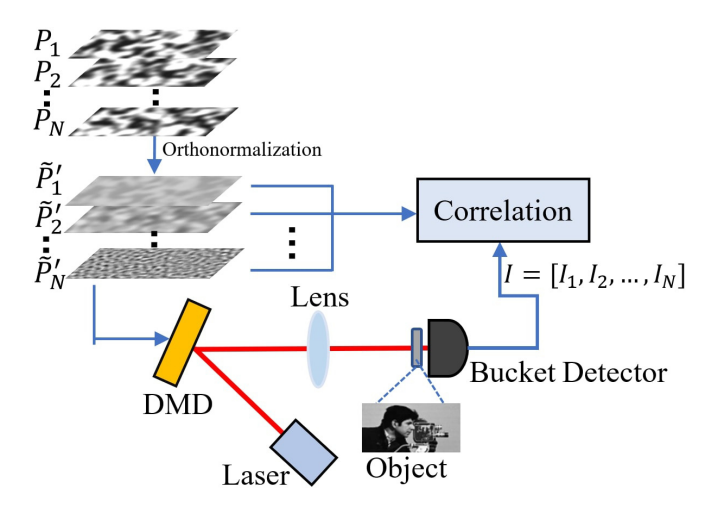


FIG. 5. Schematic of the setup. The digital micromirror device (DMD) is illuminated by a CW laser. Orthonormal patterns are loaded on the DMD and then imaged onto the object plane. Correlation measurement is made between the patterns and the intensities recorded by the bucket detector.

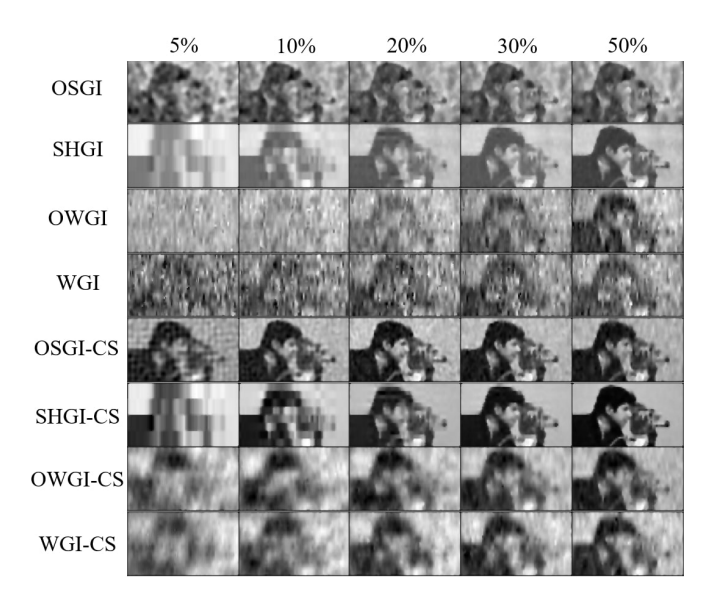


FIG. 6. Experimental results of "Cameraman" (partial) with sampling ratios from 5% to 50%. The measurement is done with various speckle patterns (OSGI, SHGI, OWGI, and WGI) and the corresponding results processed with compressive sensing algorithms. The total pixels in the image is 64×128 .

In the experiment, we measure the "cameraman" (partial) with the presence of environmental noise and the thermal noise of the detector. The noise level is measured to be $\sim 2\%$ by blocking the laser light. The exposure time of the CMOS is set to be 30 μ s. $N_{\text{pixel}} = 64 \times 128$ is used in the experiment. The main results are shown in Fig. 6. Again, OSGI already retrieves an image when β is only 5% while other methods fail. OSGI-CS improves OSGI results further by suppressing the environmental noise. SHGI and SHGI-CS can present clear images only when β reaches to 20%. It can be seen from Fig. 6 that the OSGI and OSGI-CS results have better resolution as compared to SHGI, and SHGI-CS. However, SHGI and SHGI-CS outperform in noise robustness, i.e., smoother background. This is particularly because of the binary pattern feature, which contributes a large fluctuation correlation against noise interference in the second-order measurement. We also note here that, since the SHGI uses differential patterns in real measurement [29], the number of patterns used for the measurement is actually doubled. With the presence of noise, doubled pattern numbers can also improve image quality. On the other hand, WGI and OWGI both give cognitive but very low visibility images at $\beta \sim 50\%$, and the image obtained with OWGI is clearer than WGI. OWGI-CS and WGI-CS improve the results to a visible level at $\beta \sim 50\%$, which is comparable to OSGI, but much worse than OSGI-CS, SHGI, and SHGI-CS. In a word, we can select OSGI-CS and SHGI-CS based on β to achieve the recognizable and even clear images in the sub-Nyquist sampling region. The qualities of the reconstructed images by different methods are shown in Fig. 7. As suggested by the indicator values, the experimental results with all methods are more or less affected by the experimental noise. The OSGI and OSGI-CS results are still much better in the low sampling ratio region than other methods. In particular, OSGI and OSGI-CS are better at constructing recognizable images than SHGI and SHGI-CS

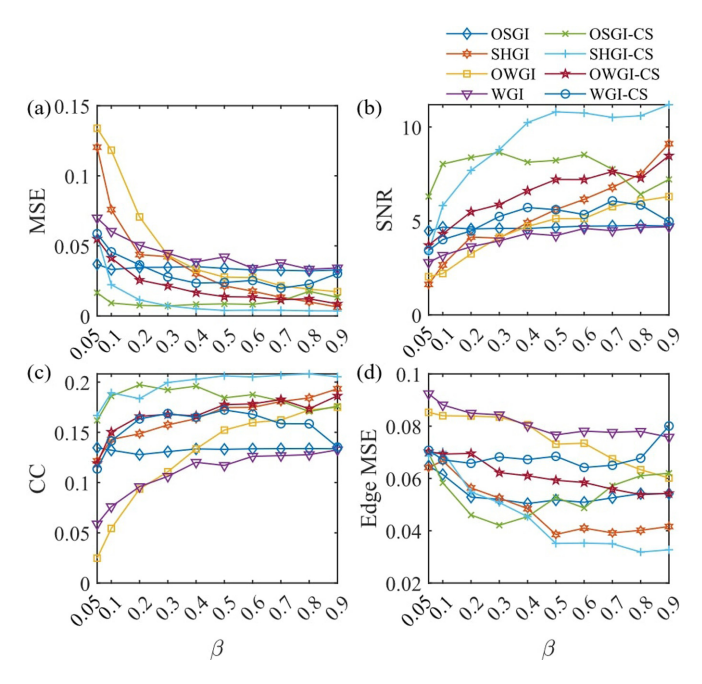


FIG. 7. Evaluation on experimental results based on the OSGI, SHGI, OWGI, WGI, OSGI-CS, SHGI-CS, OWGI-CS, and WGI-CS methods. Image qualities via different sampling ratio are given by (a) MSE, (b) SNR, (c) CC, and (d) Edge MSE.

at low sampling ratios ($\beta \le 30\%$). This is mainly because Hadamard patterns have larger individual speckles (larger than 1×1) at low β , and the orthonormal spectrum-encoded speckle patterns maintain the 1×1 individual speckle resolution. When β increases, SHGI and SHGI-CS are evaluated better than OSGI and OSGI-CS because of the extremely low noise fluctuation, as well as the doubled speckle pattern number used in the measurements. Different from the ideal case, the evaluators show that OSGI and OWGI-CS work less well at high sampling ratios. This is mainly due to the deviation from orthogonality induced by noise accumulation [21]. Some of the indicators suggest SHGI-CS gives the best result when $\beta \sim 50\%$, similar as in the simulation case. However, here OSGI-CS has the best result at $\beta \sim 20\%$. This is mainly due to the competition between the sampling ratio and the effect

of the noises. The optimal sampling ratio will move to the higher end when the noise decreases. We note here that the quality of the SHGI-CS result at $\beta=50\%$ and OSGI-CS result at $\beta=20\%$ cannot be surpassed at a nearly full sampling ratio using other conventional methods with uniformly spatial frequency distributed speckle patterns. It is also interesting to notice that the evaluators MSE and SNR, as a perception based model, are more consistent with the human vision judgment of Fig. 6, i.e., OSGI-CS has an advantage at a sampling ratio below 30%.

V. CONCLUSION AND DISCUSSION

To conclude, we developed a generally applicable orthonormal spectrum-encoded speckle pattern based on the CGI system to improve image reconstruction for low sampling ratios. Since most of the natural images are concentrated in the low spatial frequencies, the orthonormal spectrum-encoded speckle pattern is favorable in the low sampling ratio. The most significant advantage of this scheme is the continuous change of cross-correlation and the distribution in the frequency domain. This effectively reduces the sampling ratio while maintaining high image quality. We give a general way to generate this type of speckle pattern. Image quality can be improved further using the CS algorithm. It also suggests an optimal sampling ratio for the measurement when noise is present.

In addition, this method is quite analogous to the orthogonal wavelets, which also have the relationship between the spatial frequency distribution and orthogonality (orthogonal wavelets scan the frequency domain with finite bandwidth). Consequently, it can also guide ultrafast spectroscopy experiments by designing the pulse shape to acquire the spectra with the highest efficiency.

ACKNOWLEDGMENTS

This work was supported by Air Force Office of Scientific Research (Award No. FA9550-20-1-0366 DEF), Office of Naval Research (Award No. N00014-20-1-2184), Robert A. Welch Foundation (Grant No. A-1261), and National Science Foundation (Grant No. PHY-2013771).

^[1] J. H. Shapiro, Phys. Rev. A 78, 061802(R) (2008).

^[2] Y. Bromberg, O. Katz, and Y. Silberberg, Phys. Rev. A 79, 053840 (2009).

^[3] T. B. Pittman, Y. H. Shih, D. V. Strekalov, and A. V. Sergienko, Phys. Rev. A 52, R3429(R) (1995).

^[4] R. S. Bennink, S. J. Bentley, R. W. Boyd, and J. C. Howell, Phys. Rev. Lett. 92, 033601 (2004).

^[5] D. Zhang, Y.-H. Zhai, L.-A. Wu, and X.-H. Chen, Opt. Lett. 30, 2354 (2005).

^[6] M. P. Edgar, G. M. Gibson, R. W. Bowman, B. Sun, N. Radwell, K. J. Mitchell, S. S. Welsh, and M. J. Padgett, Sci. Rep. 5, 10669 (2015).

^[7] N. Radwell, K. J. Mitchell, G. M. Gibson, M. P. Edgar, R. Bowman, and M. J. Padgett, Optica 1, 285 (2014).

^[8] G. A. Howland, D. J. Lum, M. R. Ware, and J. C. Howell, Opt. Express **21**, 23822 (2013).

^[9] M.-J. Sun, M. P. Edgar, G. M. Gibson, B. Sun, N. Radwell, R. Lamb, and M. J. Padgett, Nat. Commun. 7, 1 (2016).

^[10] F. Devaux, P.-A. Moreau, S. Denis, and E. Lantz, Optica 3, 698 (2016).

^[11] Y. Klein, A. Schori, I. Dolbnya, K. Sawhney, and S. Shwartz, Opt. Express 27, 3284 (2019).

^[12] B. I. Erkmen, J. Opt. Soc. Am. A 29, 782 (2012).

^[13] O. Katz, Y. Bromberg, and Y. Silberberg, Appl. Phys. Lett. 95, 131110 (2009).

^[14] V. Katkovnik and J. Astola, J. Opt. Soc. Am. A 29, 1556 (2012).

^[15] M. Lyu, W. Wang, H. Wang, H. Wang, G. Li, N. Chen, and G. Situ, Sci. Rep. 7, 17865 (2017).

- [16] Y. He, G. Wang, G. Dong, S. Zhu, H. Chen, A. Zhang, and Z. Xu, Sci. Rep. 8, 1 (2018).
- [17] H. Wu, R. Wang, G. Zhao, H. Xiao, D. Wang, J. Liang, X. Tian, L. Cheng, and X. Zhang, Opt. Express 28, 3846 (2020).
- [18] Z. Zhang, X. Ma, and J. Zhong, Nat. Commun. 6, 1 (2015).
- [19] M.-J. Sun, L.-T. Meng, M. P. Edgar, M. J. Padgett, and N. Radwell, Sci. Rep. 7, 3464 (2017).
- [20] Z. Zhang, X. Wang, G. Zheng, and J. Zhong, Opt. Express 25, 19619 (2017).
- [21] B. Luo, P. Yin, L. Yin, G. Wu, and H. Guo, Opt. Express 26, 23093 (2018).
- [22] Z. Li, X. Nie, F. Yang, X. Liu, D. Liu, X. Dong, X. Zhao, T. Peng, M. S. Zubairy, and M. O. Scully, Opt. Express 29, 19621 (2021).

- [23] X. Nie, F. Yang, X. Liu, X. Zhao, R. Nessler, T. Peng, M. S. Zubairy, and M. O. Scully, Phys. Rev. A 104, 013513 (2021).
- [24] Z. Wang, A. C. Bovik, H. R. Sheikh, and E. P. Simoncelli, IEEE Trans. Image Process. 13, 600 (2004).
- [25] J. R. Parker, Algorithms for Image Processing and Computer Vision (Wiley, New York, 2010).
- [26] G. J. Burton and I. R. Moorhead, Appl. Opt. 26, 157 (1987).
- [27] D. L. Ruderman, Netw., Comput. Neural Syst. 5, 517 (1994).
- [28] J. Canny, IEEE Trans. Pattern Anal. Mach. Intell. PAMI-8, 679 (1986).
- [29] S. S. Welsh, M. P. Edgar, R. Bowman, B. Sun, and M. J. Padgett, J. Opt. 17, 025705 (2015).